

# Computational Simulation and Visualization of Traumatic Brain Injuries

Martin Burtscher

School of Electrical and Computer  
Engineering, Cornell University  
Ithaca, NY 14853, U.S.A.

Igor Szczyrba

Department of Mathematical Sciences  
University of Northern Colorado  
Greeley, CO 80639, U.S.A.

**Abstract** *We numerically model the human brain dynamics in realistic 2D cross-sections during traumatic scenarios corresponding to the Head Injury Criterion's critical value  $HIC_{36}=1000$ . Our simulations are based on the Kelvin-Voigt Partial Differential Equations that treat the brain tissue as a viscoelastic solid and on our nonlinear generalization of these linear PDEs that treats the tissue as an incompressible, viscoelastic fluid. To better visualize and study the brain motion, we have developed curved-vector-field plots and movies, which allow the simultaneous analysis of velocity fields with a wide range of magnitudes (as appear in turbulent flows) as well as the corresponding trajectories of brain-matter parcels. The discovered complex brain tissue oscillations shed new light on the mechanisms of Closed Head Injuries. Our results may help establish a universal brain injury tolerance criterion.*

**Keywords:** Brain injury dynamics modeling and visualization.

## 1 Introduction

Traumatic Brain Injury (TBI) is one of the most dreadful human ailments. TBI is not restricted to automotive accident victims but also affects bicyclists, skiers, and even people who just fall onto hard surfaces or ride roller coasters. *In vivo* animal TBI experiments are controversial, costly, and difficult to perform. Also, due to the differences in size, geometry, and physical properties between a human and an animal brain, it is difficult to directly apply the results obtained from animal experiments

to humans, even when merely establishing general human brain injury tolerance criteria.

Computer simulations enable consistent utilization of data obtained from medical research and experiments involving live animals, human cadavers as well as animal and human brain tissue. They also allow accounting for individual differences between people of various ages (including infants and children) and ethnic origins. Indeed, a variety of real accident scenarios and laboratory experimental settings, with different geometric and material configurations of the human or animal skull-brain system, can be numerically simulated (recreated) to validate a general TBI model against all types of data. Computational TBI models developed over the last fifteen years confirm the validity of this approach, cf. [1] and references therein.

To model the mechanisms of Diffuse Axonal Injury (DAI) that are unexplained by other TBI models, we have generalized the well-established Closed Head Injury (CHI) model that is based on the *linear* Kelvin-Voigt PDEs by introducing the following *nonlinear* PDEs describing an incompressible, viscoelastic fluid (the human brain contains circa 80% water):

$$\frac{D\mathbf{v}}{Dt} = -\nabla\tilde{p} + \Delta(c^2\mathbf{u} + \nu\mathbf{v}), \quad \frac{D\mathbf{u}}{Dt} = \mathbf{v}, \quad \nabla\cdot\mathbf{v} = 0 \quad (1).$$

Here  $D/Dt \equiv \partial/\partial t + (\mathbf{v}\cdot\nabla)$  denotes the material derivative with the velocity vector  $\mathbf{v}(\mathbf{x},t)$ ,  $\mathbf{u}(\mathbf{x},t) \equiv \mathbf{x}(\mathbf{x}_0,t) - \mathbf{x}_0$  is the Lagrangian displacement vector of a material parcel labeled by its initial position  $\mathbf{x}_0$ ,  $\tilde{p}$  is the sum of the density normalized pressure and the hydrostatic compression of solids, whereas  $c$  and  $\nu$  are

constants describing, respectively, the brain’s shear-wave phase velocity and viscosity. The Kelvin-Voigt equations are a linearized form of (1) where  $\mathbf{v} \cdot \nabla$  and  $\tilde{\rho}$  equal zero, cf. [2]

In what follows, the linear Kelvin-Voigt PDEs and our nonlinear generalization (1) of these PDEs are referred to as **L** and **NL** system/model, respectively. As it is done in the **L** and many other CHI models, in our **NL** model the severity/localizations of brain injuries are attributed to the distribution of the strain field created in the brain tissue by the shear waves.

## 2 Numerical Method

Our **NL** system is more complex than the Navier-Stokes equations and the realistic brain geometry imposes complex boundary conditions. Thus, obtaining numerical solutions requires the use of sophisticated methods. To benefit from established results, we have adapted the finite-difference code EULAG, which was developed at the National Center for Atmospheric Research in Boulder, CO, to study atmospheric and stellar phenomena [3].

The physical properties of the human brain imply that the velocity of the shear waves in the white matter equals 0.8-1.0m/s, whereas in the gray matter it is up to four times larger, cf. [4] and the references therein. Thus, the shortest shear waves that can propagate in the gray matter are longer than  $5 \cdot 10^{-3}$ m and the shortest possible shear waves in the white matter are several times longer [2]. To properly model such waves and maintain good numerical stability, we use a grid resolution  $5 \cdot 10^{-4}\text{m} \leq \Delta x \leq 2 \cdot 10^{-3}\text{m}$  and a time step  $10^{-5}\text{s} \leq \Delta t \leq 10^{-4}\text{s}$  (depending on the traumatic scenario and whether the **L** or the **NL** system is used). This amounts to up to  $16 \cdot 10^4$  calculation nodes for a 2D brain cross-section and up to  $5 \cdot 10^4$  calculation time steps.

CAT scans and MRIs provide geometrical details of brain substructures below  $10^{-3}\text{m}$ , which suffices for the accuracy required by the dispersion relations. We use cubic spline interpolations of data from medical sources to

replicate the geometry of 2D skull-brain cross-sections. Cubic splines result in differentiable curves that pass exactly through the given data points, produce natural looking, smooth 2D objects, and can be computed efficiently (in linear time with respect to the number of data points in the contours of the substructures).

Our simulations imply that  $5 \cdot 10^{-3}\text{m}$  variations in the brain shape do not affect the solutions of either PDE system in a noticeable way. It is rather global geometrical and topological properties that impact the results [5, 6]. Thus, there is no need to overemphasize the geometrical accuracy of the skull-brain facsimile. This approach is also characteristic for other computational models of brain injuries. For example, the finite-element model SIMon, developed over the last decade and continuously improved by the National Highway Traffic Safety Administration (NHTSA), includes only circa  $5 \cdot 10^3$  nodes and  $4 \cdot 10^3$  elements within the brain [1].

## 3 Curved-Vector-Field Plots

Studying brain dynamics requires a good representation of the temporal evolution of the velocity vector field within the brain. The commercially available software packages we have tested cannot depict this evolution with sufficient detail. As a remedy, we have developed curved-vector-field (CVF) plots, which can readily be converted into MPEG movies. In comparison to typical vector plots, CVF plots use shaded lines instead of arrows to indicate the direction of the vectors. This approach allows to display many more vectors in the same plot without cluttering it and thus better portrays fields with highly varying magnitudes and directions. Moreover, CVF plots utilize curved instead of straight vectors to more clearly visualize the trajectories of the brain parcels, especially in turbulent fields. As a consequence, our plots make important subtleties obvious and thus enable a better understanding of possible CHI mechanisms.

To construct CVF plots, we start the vectors in the grid points whose integer coor-

ordinates  $(i, j)$  lie inside of the brain cross-section and satisfy  $i \bmod n = 0$ ,  $j \bmod n = 0$ , and  $(i+j) \bmod n \bmod 2 = 0$ , where  $n$  controls the density of the plot. In other words, we select every  $n^{\text{th}}$  row and column from the grid and then alternately drop the even and odd points from the selected rows (or columns). Alternating between even and odd points results in a visually more appealing plot. The points that remain become the origins of the curved vectors, which are drawn as follows.

First, the current position  $(x, y)$  is set to the origin. Next we repeat the following steps  $m$  times, where  $m$  is the number of straight-line segments used to approximate each curved vector. We pick the four points in the grid that are closest to the current position. Using simulation data from these four points, we compute bi-linear interpolations to obtain results for the current position  $(x, y)$ . The interpolated results are then scaled by a user-provided constant factor to stretch (or shrink) all vectors to a visually pleasing length.

Then we add the scaled values to the current position, yielding a new position, and draw a straight-line segment from the current to the new position. The first segment is the darkest and each consecutive segment is somewhat lighter. This gradual shading indicates the direction of the vector. Finally, the new position becomes the current position. We repeat the above steps until  $m$  segments have been plotted. This algorithm is applied to each vector. Once all the curved vectors have been drawn, we add an outline of the brain contour to complete the CVF plot.

## 4 Simulation Setup

The analytic solutions of the  $\mathbf{L}$  system for impulsively rotated, idealized (cylindrical and spherical) skull shapes reveal simple oscillations of the brain matter with sufficiently large strain values to rupture veins or damage neurons. These solutions have been used to predict the occurrences of subdural hematoma and to create a Diffuse Axonal Injury criterion [7, 8],

but they are insufficient for determining even general localization of injuries within the brain.

Our simulations of the brain dynamics within 2D cross-sections after an impulsive skull movement showed that realistic brain shapes and physical properties lead to complicated oscillations that could explain the general localization of injuries [5, 6, 9, 10]. However, since these simulations use rectangularly shaped accelerations occurring within one time step  $\Delta t \leq 10^{-4}$ s, it is difficult to compare their results with experimental brain injury criteria. Indeed, the NHTSA assesses brain injuries occurring as a result of *translational* accelerations by means of the Head Injury Criterion [11]:

$$\text{HIC}_{1000(t_2-t_1)} = \max \left[ \frac{1}{(t_2-t_1)} \int_{t_1}^{t_2} a(t) dt \right]^{2.5} \cdot (t_2-t_1),$$
where  $a(t)$  is the head's translational acceleration in  $g$ 's and (to get reliable predictions) the length  $T=t_2-t_1$  of the time intervals  $[t_1, t_2]$ —over which the maximum is calculated—is assumed to be in the range  $10^{-3}\text{s} \leq T \leq 10^{-1}\text{s}$ .

Thus, to model the 2D brain dynamics that results from a traumatic translation (assumed to be *from left to right*), we reduce the initial constant skull velocity  $v_0 = \alpha(T/2)^2$  using the triangularly shaped scalar deceleration:

$$\begin{aligned} a(t) &= -\alpha t && \text{for } 0 \leq t \leq T/2, \\ a(t) &= \alpha t - \alpha T && \text{for } T/2 < t < T, \\ a(t) &= 0 && \text{for } T \leq t \end{aligned} \quad (2)$$

with  $\alpha = 65400\text{m/s}^3$  and  $T = 36 \cdot 10^{-3}\text{s}$  leading to  $v_0 = 21.2\text{m/s}$  and  $\text{HIC}_{36} = 1000$ , i.e., the HIC value associated with severe brain injuries [11].

To properly compare all results, we assume the transfer of power from the skull to the brain in our *rotational* decelerations to be the same as in the translational decelerations described above. Thus, for a cross-section with 'radius'  $r$  whose 'center' is distanced from the axis of rotation by  $R$ , we use the initial *clockwise* angular velocity  $\omega_0 = v_0 / \sqrt{r^2 + R^2}$  with the same  $v_0$  as above and the angular deceleration  $d\omega(t)/dt = a(t) / \sqrt{r^2 + R^2}$  with  $a(t)$  given by (2). Consequently, the largest initial tangential velocity  $v$  (e.g., at the top of the head) is equal to  $v_0(r+R) / \sqrt{r^2 + R^2}$ , and  $v$  assumes the maximum value of  $\sqrt{2}v_0$  if  $R=r$ , i.e., for a rotation about the skull's base.

## 5 Results

To investigate the extent to which the features of the solutions—and hence the localization and severity of potential brain injuries—depend on the traumatic motion’s type and the brain’s geometry/topology, we conducted simulations involving sagittal brain cross-sections as well as horizontal brain cross-sections with and without the *falx cerebri*. When modeling rotational decelerations of the skull, we position the axis at the brain’s ‘center’, the skull’s base, the neck, the abdomen, etc.

Our simulations with both PDE systems show that just after the skull deceleration begins, the brain matter ‘attempts’ to maintain its initial velocity (as expected). However, the incompressibility condition  $\nabla \cdot \mathbf{v} = 0$  in (1) does not allow the creation of any void between the brain and the skull. Therefore, this initial brain matter movement transforms into a rotational motion with respect to the skull (regardless of whether the skull is slowed down by a rotational or translational deceleration). Since the brain tissue is elastic, the rotational motion within the brain leads to oscillations relative to the decelerating skull, which are damped by the brain’s viscosity. The specific character of these complicated oscillations depends on the geometry and topology of the cross-section, the type of motion, and the PDE system used.

Fig. 1 depicts the **L** system’s velocity field evolution in a sagittal brain cross-section whose initial rotation about its center is decelerated. After a short initial surge of circular clockwise motion (due to the diminishing skull velocity), the brain matter bounces back and then forth. The noncircular boundary quickly distorts this initial oscillation and a multi-vortex pattern arises shortly after  $a(t)$  assumes its extremum at  $t=0.018\text{s}$  (top). 0.01s later, two vortices emerge (middle) with diminishing velocities (shorter curved vectors), and after the skull stops at  $t=0.036\text{s}$  the boundary-following pattern is restored (bottom). Multi-vortex oscillations continue in the resting skull for tens of milliseconds with smaller and smaller velocities and amplitudes.

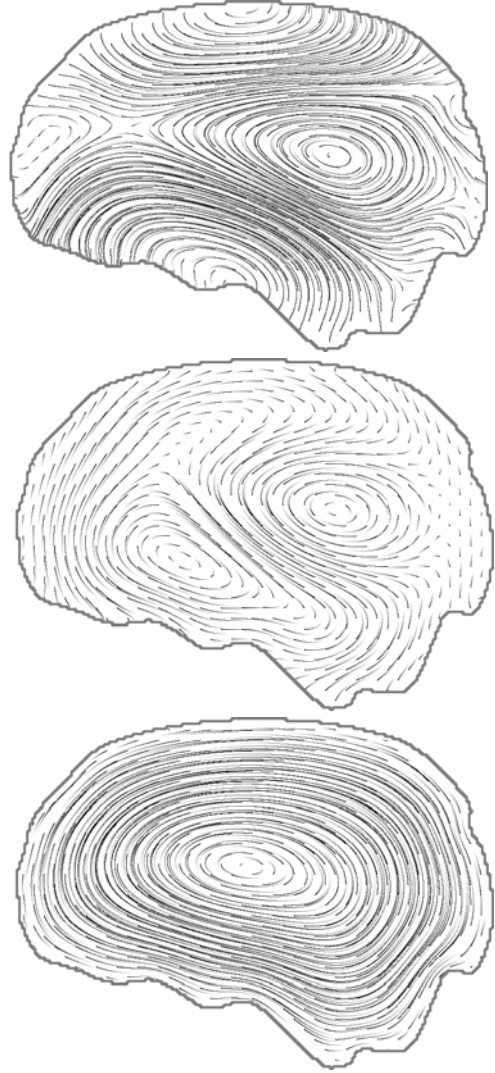


Figure 1:

The **L** system’s velocity field in a sagittal cross-section at  $t=0.02\text{s}$ ,  $0.03\text{s}$ , and  $0.04\text{s}$ , resp., from top to bottom; central rotation.

If the sagittal cross-section is translated instead of rotated, the first oscillatory vortex begins to form only at  $t=0.015\text{s}$ , and for  $t \geq 0.03\text{s}$  the brain matter motion evolves into a multi-vortex oscillation, Fig. 2. For a fixed  $t$ , the oscillatory patterns from Fig. 2 gradually ‘transition’ to the corresponding patterns in Fig. 1 as we move the axis of rotation closer to the cross-section’s ‘center’ (i.e., as we decrease  $R$ ).

The introduction of nonlinearity leads to turbulence that distorts (especially for larger  $R$ ’s) the oscillatory patterns appearing in the **L** case. Fig. 3 depicts the **NL** system’s velocity field in the translated (top panels) and rotated

(bottom panels) sagittal cross-section. Again, when radius  $R$  is varied, transitional patterns arise that ‘link’ the top and bottom patterns.

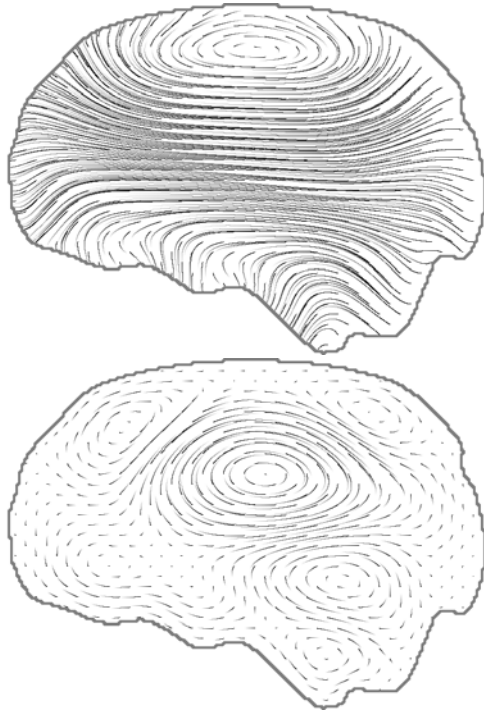


Figure 2:

The  $\mathbf{L}$  system’s velocity field in a sagittal cross-section at  $t=0.02\text{s}$  (top) and at  $t=0.04\text{s}$  (bottom); translation.

Comparing central rotations of sagittal and (more symmetric) horizontal cross-sections enables us to gauge to which extent the domain’s shape and topology impact the solutions of each system. Fig. 4 shows the  $\mathbf{L}$  system’s velocity field in a rotated horizontal cross-section without the *falx cerebri*. In this case, the boundary-following pattern of oscillations is not disturbed essentially during the deceleration (Fig. 4, left). However, when the skull comes to rest, a layer of vortices forms near the skull that then ‘moves’ towards the center (Fig. 4, right). Similar ‘elliptic’ oscillatory patterns appear also in the  $\mathbf{NL}$  case with minor turbulent perturbations near the skull.

Contrary to the sagittal cross-section, the translation of a horizontal cross-section without the *falx cerebri* based on the  $\mathbf{L}$  system leads to symmetric oscillatory patterns after skull rests, cf. Fig. 5 (left) and Fig. 2 (bottom). Non-

linearity violates this symmetry due to a turbulent flow that allows to determine the direction of the skull’s motion, Fig. 5, right.

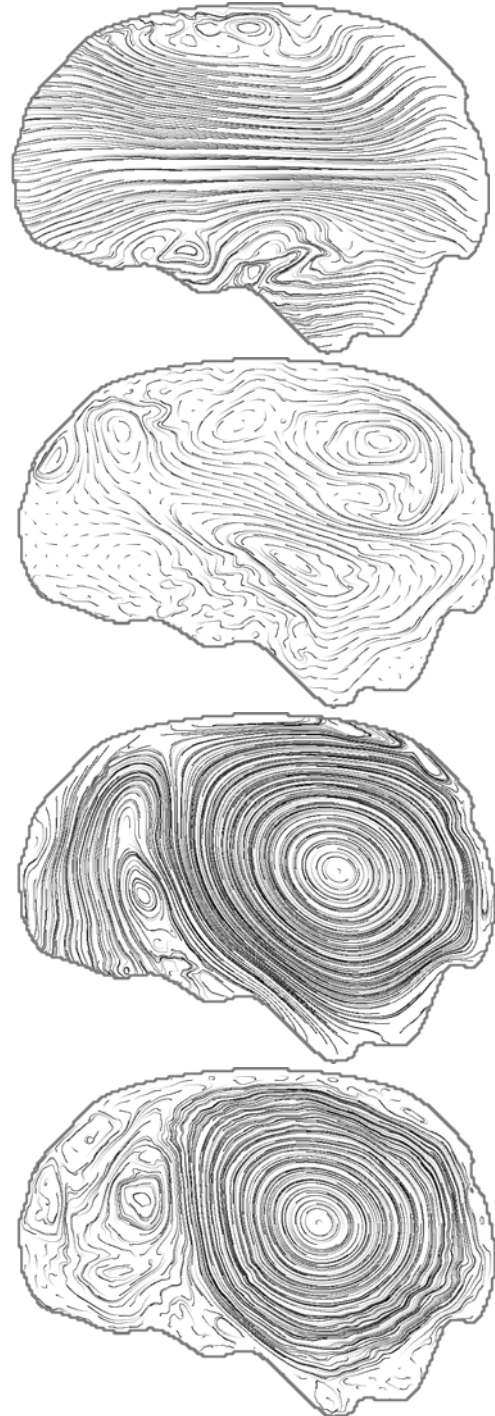


Figure 3:

The  $\mathbf{NL}$  system’s velocity field in a sagittal cross-section at  $t=0.02\text{s}$  (top and third) and at  $t=0.04\text{s}$  (second and bottom); translation (top two); rotation (bottom two).

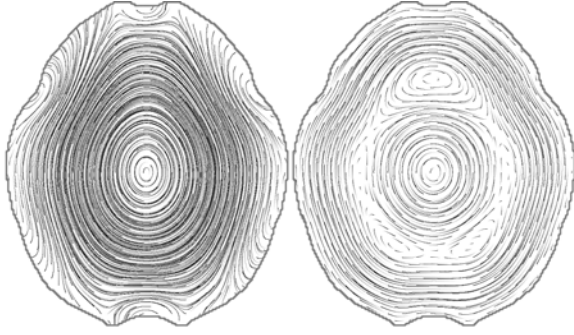


Figure 4:

The **L** system's velocity field in a horizontal cross-section without *falx cerebri* at  $t=0.02s$  (left) and at  $t=0.04s$  (right); central rotation.

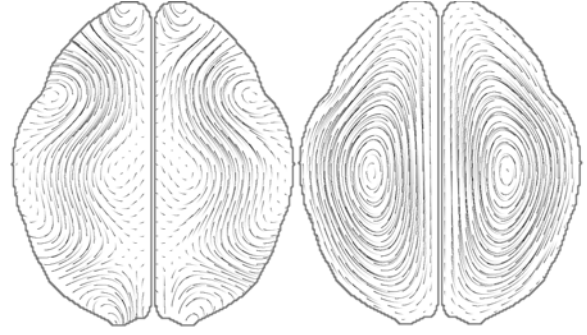


Figure 6:

The **L** system's velocity field in a horizontal cross-section with *falx cerebri* at  $t=0.02s$  (left) and at  $t=0.04s$  (right); central rotation.

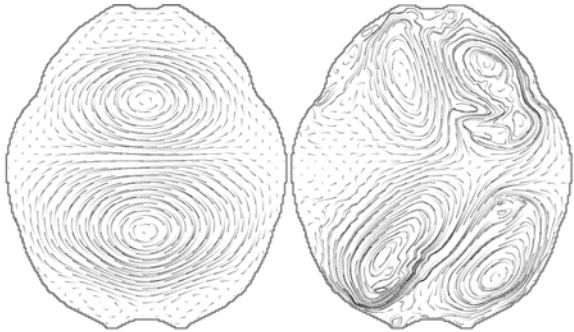


Figure 5:

Velocity fields in a horizontal cross-section without *falx cerebri* at  $t=0.04s$ ; **L** system (left) and **NL** system (right); translation.

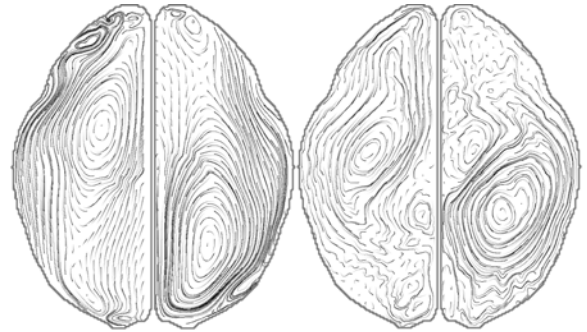


Figure 7:

The **NL** system's velocity field in a horizontal cross-section with *falx cerebri* at  $t=0.02s$  (left) and at  $t=0.04s$  (right); central rotation.

Figs. 6 and 7 depict, respectively, the **L** and **NL** systems' velocity fields in a centrally rotated horizontal cross-section separated by the *falx cerebri*. In the **L** case, the *falx cerebri* modifies essentially the character of the solution during the rotation (compare the left panels of Figs. 4 and 6), but the skull's rotational direction still cannot be easily determined. The boundary-following pattern of brain oscillations (cf. Fig. 6, right) is restored already before the skull rests. In the **NL** case, the presence of the *falx cerebri* greatly impacts the solution's mirror symmetry (Fig. 7) and, contrary to the case without the *falx cerebri* (not shown), the turbulent flow again allows to determine the rotational direction.

Similar to the case without the *falx cerebri*, a translation of the horizontal cross-section with the *falx cerebri* leads to symmetric oscillatory patterns in the **L** case and to asymmetric pat-

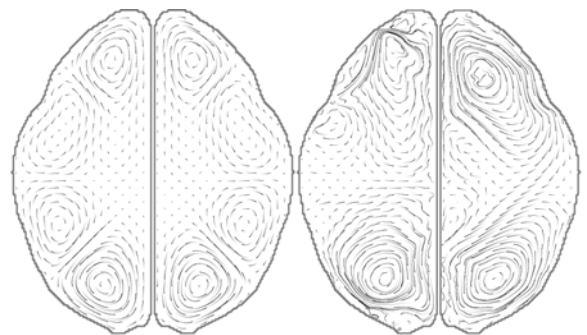


Figure 8:

Velocity fields in a horizontal cross-section with *falx cerebri* at  $t=0.04s$ ; **L** system (left) and **NL** system (right); translation.

terns in the **NL** case, although the violation of symmetry is mitigated by the presence of the *falx cerebri*, compare both right Figs. 8 and 5.

More detailed information is available at <http://www.csl.cornell.edu/~burtscher/CHI-research/> in form of MPEG movies.

## 6 Conclusions

The Head Injury Criterion's critical values are well established for translational head decelerations [11], but it is not clear how to apply them in the case of traumatic rotations. Our results validate the correctness of our approach, which uses the transfer of an *equal* amount of power from the skull to the brain as a common denominator, thus allowing to properly compare the consequences of arbitrary traumatic head motions. Indeed, our results show that under this assumption, the translational solutions 'transition' into central rotational solutions.

The observed brain oscillations create complex multi-vortex patterns whose form depends on the PDEs used and the type of motion, including the position of the rotational axis (e.g., brain center, neck, or infinity-translation). Since the brain matter movement near vortices usually leads to high values of strain, the locations of the vortices represent potential sites for brain injuries. Consequently, our results imply that it is rather unrealistic to expect that any CHI model can predict the exact localization of brain injuries without very precise information about the head's motion.

The general features of the oscillations induced by triangularly shaped head decelerations are similar to those appearing after impulsive motions [5, 6]. Hence, the known fact that the specific shape of a translational deceleration associated with a given HIC value is not a decisive factor for causing a severe brain injury may also be valid for rotational decelerations. Thus, our results indicate that a universal Brain Injury Criterion for arbitrary head motions (similar to the HIC) can be derived.

Our discovery that complicated brain matter oscillations tend to continue *after* rapid head decelerations implies that the brain might sustain traumatic damage not only during the head motion but also when the head already rests. Consequently, a repetitive head motion (appearing, e.g., when boxing or shaking babies) can lead to a severe brain injury due to resonance effects even if each individual head movement is 'non-traumatic'.

## References

- [1] E. G. Takhounts *et al.* On the Development of the SIMon Finite Element Model, *Stapp Car Crash J.*, 47:107-133, 2003.
- [2] C. S. Cotter, P. K. Smolarkiewicz and I. N. Szczyrba, A Viscoelastic Model for Brain Injuries. *Int. J. for Numerical Methods in Fluids*, 40:303-311, 2002.
- [3] J. M. Prusa and P. K. Smolarkiewicz, An All-Scale Anelastic Model for Geophysical Flows: Dynamic Grid Deformation, *J. Comp. Phys.*, 190:601-622, 2003.
- [4] E. G. Takhounts *et al.* On the Importance of Nonlinearity of Brain Tissue Under Large Deformations, *Stapp Car Crash J.* 47:79-92, 2003.
- [5] M. Burtscher and I. Szczyrba, Numerical Modeling of Brain Dynamics in Traumatic Situations – Impulsive Translations, *Proc. METMBS'05*:205-211, CSREA Press.
- [6] M. Burtscher and I. Szczyrba, On the Role of the Brain's Geometry in Closed Head Injuries, *Proc. 2005 Bioengin. Conf.*
- [7] C. Ljung. A Model for Brain Deformation Due to Rotation of the Skull. *J. Biomech.*, 8:263-274, 1975.
- [8] S. S. Margulies and L. Thibault. A Proposed Tolerance Criterion for Diffuse Axonal Injury in Man. *J. Biomech.*, 25:917-923, 1992.
- [9] I. Szczyrba *et al.* Numerical Simulations of Closed Head Injuries, *Proc. METMBS'02*, 2:486-492, CSREA Press.
- [10] I. Szczyrba and M. Burtscher, On the Role of Ventricles in Diffuse Axonal Injuries, *Proc. 2003 Bioengin. Conf.*, 147-148.
- [11] M. Kleinberger *et al.* 1998. Development of Improved Injury Criteria for the Assessment of Advanced Automotive Restraint Systems, NHTSA, <http://www-nrd.nhtsa.dot.gov/pdf/nrd-11/airbags/criteria.pdf>